ARTICLE OPEN

Single-nanometer CoFeB/MgO magnetic tunnel junctions with high-retention and high-speed capabilities

Junta Igarashi[1,2,3,8], Butsurin Jinnai[4,8]✉, Kyota Watanabe[1,3], Takanobu Shinoda[1,3], Takuya Funatsu[1,3], Hideo Sato[1,5,6], Shunsuke Fukami[1,3,4,5,6,7]✉ and Hideo Ohno[1,3,4,5,6]

Making magnetic tunnel junctions (MTJs) smaller while meeting performance requirements is critical for future electronics with spin-transfer torque magnetoresistive random access memory (STT-MRAM). However, it is challenging in the conventional MTJs using a thin CoFeB free layer capped with an MgO layer because of increasing difficulties in satisfying the required data retention and switching speed at smaller scales. Here we report single-nanometer MTJs using a free layer consisting of CoFeB/MgO multilayers, where the number of CoFeB/MgO interfaces and/or the CoFeB thicknesses are engineered to tailor device performance to applications requiring high-data retention or high-speed capability. We fabricate ultra-small MTJs down to 2.0 nm and show high data retention (over 10 years) and high-speed switching at 10 ns or below in sub-5-nm MTJs. The stack design proposed here proves that ultra-small CoFeB/MgO MTJs hold the potential for high-performance and high-density STT-MRAM.

npj Spintronics (2024)2:1 ; https://doi.org/10.1038/s44306-023-00003-2

INTRODUCTION

Spin-transfer torque magnetoresistive random access memory (STT-MRAM)[1–6] has been developed for a wide range of applications, such as buffer memory[7,8], IoT[9,10]/AI[11,12], and automobile[13–15]/space[16,17], by replacing the existing SRAM, DRAM[18,19], and Flash memories. The development of magnetic tunnel junction (MTJ), a storage component of STT-MRAM, requires tailoring its performance to such application requirements. MTJ is engineered mainly in two directions: for SRAM-like and Flash-like applications, where fast speed and long data retention are critical, respectively. In addition, like other electronics components, MTJ development has always come along with a challenge in scalability[20]. The MTJ consists of a thin tunnel barrier sandwiched by two ferromagnetic layers (free and reference layers) and engineering of the stack design enables MTJ performance to meet requirements in a variety of applications[13,21–23]. Because of superiority in writing efficiency[24] and scalability[20] as well as the compatibility with the CMOS integration process, currently developed MTJs are based on CoFeB/MgO material system with a perpendicular magnetic anisotropy, which originates from interfacial anisotropy at the CoFeB/MgO interface[25]. To improve MTJ performance, the interfacial anisotropy is enhanced by capping a CoFeB free layer with another MgO layer[26] and/or inserting an MgO layer into a CoFeB free layer[27]. These so-called interfacial-anisotropy MTJs have demonstrated scaling down to 1X nm[26–29] and have been commercialized with a diameter of several tens of nanometers by semiconductor foundries[30–32]. However, scaling beyond 10 nm (single nanometer) is challenging with the interfacial-anisotropy MTJ due to insufficient retention performance[28]. To address this issue, the MTJ that relies on not only interfacial anisotropy but also perpendicular shape anisotropy by making the CoFeB free layer thick at ultra-small scale has been proposed and its basic operation was demonstrated down to 3.8 nm in diameter[33]. However, the so-called shape-anisotropy MTJ[33,34], while showing high retention performance at ultrasmall scale, is difficult to achieve fast STT switching due to increasing switching current at a shorter timescale as described later in detail.

In this Article, we report single-nanometer MTJs using a multilayered ferromagnetic structure as a free layer, whose performance can be tailored for both speed- and retention-critical applications. The multilayered ferromagnetic structure uses the conventional CoFeB/MgO material system without resorting to new materials but consists of multiple CoFeB/MgO layers. This enables independent control of shape and interfacial anisotropies, which determine retention and/or switching performance. We demonstrate sub-ten-ns STT switching and over-10-year retention individually in single-nanometer MTJs with different stack designs.

RESULTS

Design of CoFeB/MgO multilayers as a free layer

The CoFeB/MgO multilayers consist of multiple CoFeB/MgO layers, i.e., [CoFeB(t_{CoFeB})/MgO]$_N$, where each CoFeB thickness t_{CoFeB} and the repetition N of CoFeB/MgO layers can be varied (Fig. 1a). This enables independent control of interfacial and shape anisotropies, determining factors for retention and switching speed performance as explained later. Multiple CoFeB layers in the free layer are strongly coupled through a magnetostatic interaction that becomes evident by shrinking the MTJ sizes and behaves as a single ferromagnet[35] while exchange coupling that was reported to exist in previous studies[27,36] may have some effect in our system as well. The total thickness of the multiple CoFeB layers accounts for shape anisotropy; increasing t_{CoFeB} enhances the total anisotropy. Note that each CoFeB thickness is limited to 15 nm, beyond which may cause an incoherent reversal[37,38] while coherent magnetization reversal is confirmed with 15-nm CoFeB layer[39]. On the other hand, interfacial anisotropy is effectively

[1]Laboratory for Nanoelectronics and Spintronics, Research Institute of Electrical Communication, Tohoku University, Sendai 980-8577, Japan. [2]Institut Jean Lamour, UMR CNRS 7198, Université de Lorraine, Nancy 54011, France. [3]Graduate School of Engineering, Tohoku University, Sendai 980-0845, Japan. [4]WPI-Advanced Institute for Materials Research, Tohoku University, Sendai 980-8577, Japan. [5]Center for Science and Innovation in Spintronics, Tohoku University, Sendai 980-8577, Japan. [6]Center for Innovative Integrated Electronic Systems, Tohoku University, Sendai 980-0845, Japan. [7]Inamori Research Institute for Science, Kyoto 600-8411, Japan. [8]These authors contributed equally: Junta Igarashi, Butsurin Jinnai. ✉email: butsurin@tohoku.ac.jp; s-fukami@tohoku.ac.jp

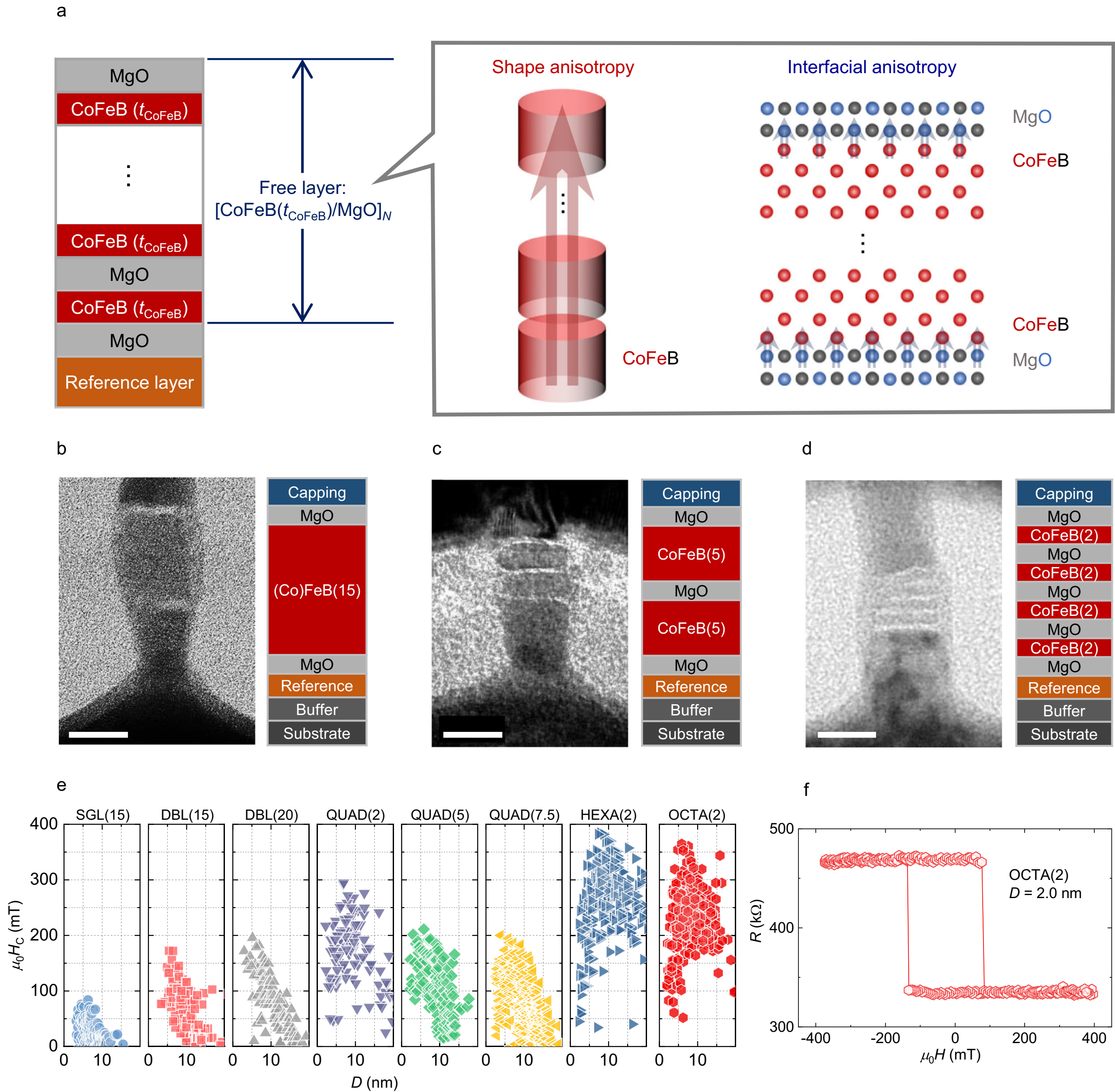

Fig. 1 Concept of single-digit nanometer MTJs for various applications. **a** Stack structure of studied MTJ with schematic illustration of design principle. **b**–**d** TEM images of studied MTJs for (**b**) DBL(15) (ref. [33]), (**c**) QUAD(5), and (**d**) OCTA(2). The white line in Fig. 1b, 1c, and 1d is a 10 nm scale bar. **e** Summary of coercive field μ_0H_C for studied MTJs. **f** *R-H* curve for OCTA(2) with $D = 2.0$ nm. TEM image of DBL(15) in (**b**) is reproduced from ref. [33]. Copyright 2018 Author(s), licensed under a CC BY license. A part of data in (**e**) is reproduced with permission from ref. [35]. Copyright 2020 IEEE; ref. [40]. Copyright 2021 IEEE.

enhanced by increasing N[40], and the contribution of interfacial anisotropy becomes more significant than that of shape anisotropy by reducing t_{CoFeB}. In the following, we show a design principle using the CoFeB/MgO multilayers to tailor its performance specialized for retention or speed.

Retention property is measured as thermal stability factor Δ, which, assuming coherent reversal in a ferromagnet, is expressed as

$$\Delta = \frac{E}{k_BT} = \frac{K_{eff}t}{k_BT}\frac{\pi D^2}{4}, \quad (1)$$

$$K_{eff} = \frac{M_SH_K^{eff}}{2} = K_b + \frac{K_i}{t} - \delta N\frac{M_S^2}{2\mu_0}, \quad (2)$$

where E is an energy barrier between two magnetization states; k_B the Boltzmann constant; T the absolute temperature; K_{eff} the effective magnetic anisotropy energy density; D the free-layer diameter; H_K^{eff} the effective magnetic anisotropy field; K_b the bulk (magnetocrystalline) anisotropy energy density; K_i the interfacial anisotropy energy density; t the ferromagnet thickness; δN the difference in the dimensionless demagnetization coefficients, or the shape anisotropy coefficient, between the perpendicular and in-plane orientations; M_S the spontaneous magnetization; and μ_0 the permeability in free space. As in Eq. (1), Δ is proportional to $K_{eff}tD^2$. Since the required Δ is determined by applications and D scales down with technology nodes, one can only adjust $K_{eff}t$. As K_b in the CoFeB/MgO material system is negligibly small[25], increasing Δ needs the enhancement of interfacial and/or shape

anisotropies, corresponding to the second and third terms in Eq. (2), respectively.

The MTJ for retention-critical applications does not require high-speed operation and switching within several tens of ns is acceptable. On the other hand, it requires a high retention property at a wide range of temperatures; for example, automobile applications demand 10-year retention at −40 to 150°C[41], and embedded memory applications, where the program code is loaded in the chip before soldering, require data retention during 260°C reflow process corresponding to 10-year retention at 225°C[42,43]. This means that the retention property has to be insensitive to temperature. According to previous works, shape-anisotropy MTJ shows smaller changes in E and coercivity with T compared to interfacial-anisotropy MTJ because K_{eff} of the former (latter) is mainly governed by M_S (K_i), which is relatively T-insensitive (sensitive) for the CoFeB/MgO systems[44–47]. Therefore, the free layer needs to be thick so that temperature-insensitive shape anisotropy can be dominant.

For the speed-critical applications, switching voltage V_C at a short pulse duration τ_p typically less than 10 ns is required, while the retention requirement is relaxed to several seconds to months. At short τ_p, or in a precessional regime[1,4,48–50], where switching is determined by the dispersion of the initial magnetization angle due to the thermal fluctuation and the transferred total angular momentum with the negligible role of thermal fluctuation[51], V_C, at which switching probability P_{SW} is 0.5, increases in inversely proportional to τ_p as[1,48–50,52]

$$V_C = V_{C0}\left\{1 + \left(\frac{\tau_D}{\tau_p}\right)\frac{\ln[4\Delta/\ln 2]}{2}\right\}, \tag{3}$$

$$V_{C0} = \frac{2\alpha e\Delta k_B T}{g_{STT}}\frac{4}{\pi D^2}RA, \tag{4}$$

$$\tau_D = \frac{1+\alpha^2}{\alpha\gamma\mu_0 H_K^{eff}}, \tag{5}$$

where V_{C0} is intrinsic critical voltage, α the damping constant, e the elementary charge, $\hbar$ the Dirac constant, g_{STT} the STT efficiency, γ the gyromagnetic ratio, and τ_D the characteristic relaxation time. τ_D determines the switching time scale in this regime[4] and should be lowered to suppress the V_C increases with reducing τ_p. This can be achieved by increasing H_K^{eff} [see Eq. (5)][4,53], and in this regard, MTJs with shape anisotropy, whose Δ mostly relies on t, is unfavorable, as they have smaller K_{eff}. Therefore, lowering t and increasing K_{eff}, i.e., increasing the interfacial (or bulk) anisotropy, are the design principles for fast switching. In addition to switching speed, we have confirmed that t should be thinner than 20 nm for STT switching in our shape-anisotropy MTJs (see Supplementary Information S1 for STT switching in shape-anisotropy MTJs). Note that increasing α also shortens τ_D, but there is a trade-off as V_{C0} is proportional to α (see Supplementary Information S2 for calculation of τ_D with different α values).

Fabrication of single-nanometer MTJs with CoFeB/MgO multilayers

Following the design guide presented in the previous section, we fabricate the MTJs with various t_{CoFeB} and N using the multilayered ferromagnetic structure as a free layer. The stack structures fabricated in this work are summarized in Table 1. Here, MTJs with $N = 1$, 2, 3, and 4 are referred to as DBL, QUAD, HEXA, and OCTA, respectively[35,40]. We also fabricate the MTJ with a 15-nm CoFeB free layer capped by a Ta layer (SGL(15)) for comparison. See Methods for more information about MTJ fabrication. Note that the contribution of shape (interfacial) anisotropy becomes less (more) dominant at $t < D$. Fig. 1b–d shows transmission electron microscopy (TEM) images for DBL(15), QUAD(5), and OCTA(2), respectively. Bright layers and dark layers in between bright layers correspond to MgO and CoFeB layers, respectively. Small MTJs down to 2.0 nm in diameter are fabricated for various structures listed in Table 1. Fig. 1e shows coercivity $\mu_0 H_C$ with respect to D for studied structures and Fig. 1f shows MTJ resistance R as a function of external magnetic field H for OCTA(2) with $D = 2.0$ nm. For further measurements to investigate the thermal stability factor Δ and STT switching property, we choose devices whose H_C is close to the average so that they represent typical device properties for each structure. Regarding tunnel magnetoresistance (TMR) ratio, we confirmed that the TMR ratio decreases with increasing N, possibly due to parasitic resistance from the inserted MgO layer in the multilayer[40]. As demonstrated in previous works[27,29], optimizing the MgO layer could address this issue.

Single-nanometer MTJs with high data retention capability

We study retention property in the fabricated MTJs based on the stack design principle described in the previous section. First, we characterize Δ at RT by measuring switching probability under a magnetic field. The obtained Δ at RT is summarized in Fig. 2a. Δ is enhanced by increasing N from SGL(15) to DBL(15) to QUAD(7.5) even with the same total CoFeB thickness and also by increasing t_{CoFeB} from QUAD(2) to QUAD(5) and QUAD(7.5) even with the same N, indicating the positive effects of the interfacial and shape anisotropies. Δ of QUAD(5) and QUAD(7.5) is comparable with that of DBL(15) and DBL(20), respectively. This means that inserting an MgO layer enables to reduce the required thickness by about 5 nm, which is beneficial for fast STT switching as described earlier[35,37,38]. For the MTJs with total CoFeB thickness below 10 nm or with interfacial anisotropy enhanced, such as QUAD(2), HEXA(2), and OCTA(2), Δ over 50 is obtained even below 5 nm[40].

We then measure the temperature dependence of Δ in QUAD(5) and QUAD(7.5) with $D \sim 7$ nm (Fig. 2b) to examine high-temperature capability. For comparison, we also plot Δ for DBL(15) with $D = 8.4$ nm from the previous study[44]. Δ over 70 at 150 °C is obtained in QUAD(7.5)[35]. From the temperature dependence of Δ, we can obtain scaling exponent n, which characterizes temperature dependence of Δ or E[44,54] (see Methods

Table 1. Information of studied samples.

Sample notation	Free-layer structure	No. of CoFeB/MgO interfaces	No. of MgO layers	Total CoFeB thickness (nm)	RA (Ωμm²)
SGL(15)	CoFeB(15)	1	1	15	2.8
DBL(15)	$[CoFeB(15)/MgO(0.93)]_1$	2	2	15	5.4 and 3.1
DBL(20)	$[CoFeB(20)/MgO(0.93)]_1$	2	2	20	2.1
QUAD(2)	$[CoFeB(2)/MgO(0.93)]_2$	4	3	4	1.0
QUAD(5)	$[CoFeB(5)/MgO(0.93)]_2$	4	3	10	1.9
QUAD(7.5)	$[CoFeB(7.5)/MgO(0.93)]_2$	4	3	15	1.9
HEXA(2)	$[CoFeB(2)/MgO(0.93)]_3$	6	4	6	1.2
OCTA(2)	$[CoFeB(2)/MgO(0.93)]_4$	8	5	8	1.0, 1.2, and 1.7

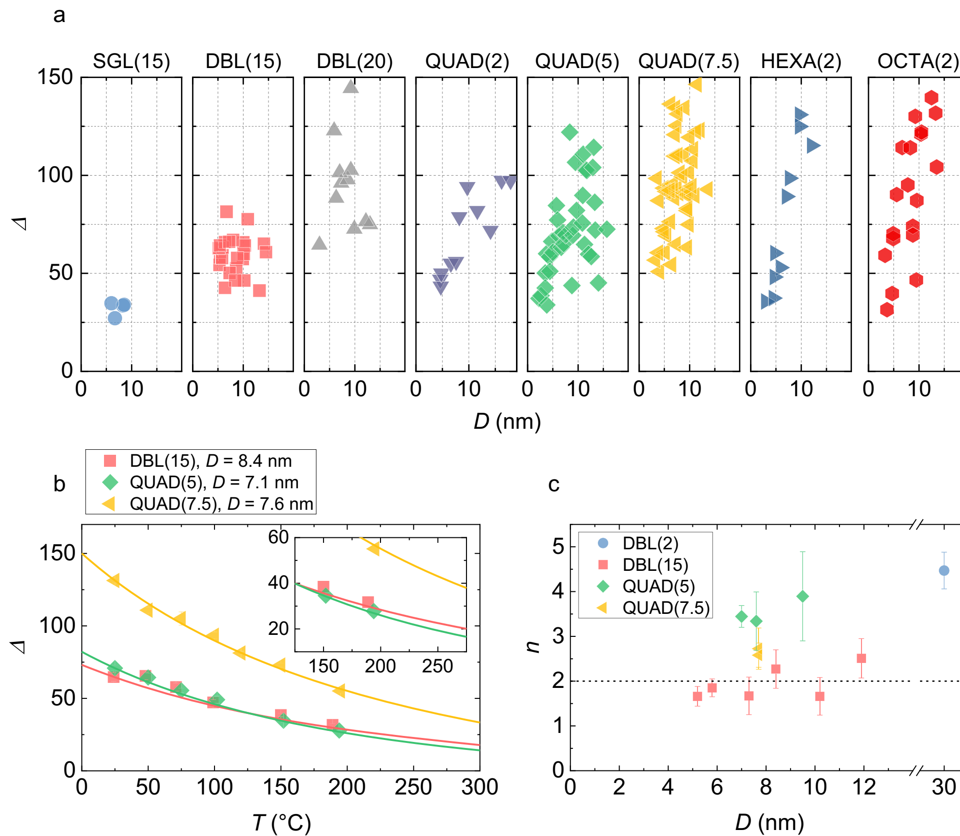

Fig. 2 Evaluated retention properties for studied MTJs. a Obtained Δ with respect to D in MTJs for studied MTJs. **b** Temperature dependence of Δ for QUAD(5) and QUAD(7.5) with $D \sim 7$ nm. Curves are calculation based on power law scaling relationship between E and M_S with obtained n values (see Methods for more details). The inset shows an enlarged figure. **c** Summary of exponent n for DBL(15), QUAD(5), QUAD(7.5), and interfacial-anisotropy MTJ for comparison. The error bar shows the standard error of fitting Eq. (7) to the experimental results. A part of data in (**a**) and (**b**) is reproduced with permission from ref. [35]. Copyright 2020 IEEE; ref. [40]. Copyright 2021 IEEE. A part of data in (**b**) and (**c**) is reproduced with permission from ref. [44]. Copyright 2021 AIP Publishing LLC.

for more information). Note that the smaller the n values are, the weaker the temperature dependence of Δ or E becomes, which is preferable for high-temperature applications. Fig. 2c summarizes n values for various structures. For comparison, we also plot n for DBL(15) and interfacial-anisotropy MTJ with a free layer of CoFeB(2)/MgO (DBL(2)) from previous studies[44,54]. Increasing total t_{CoFeB} or decreasing N makes the n values smaller, i.e., temperature insensitive, and close to 2 as a result of the decrease (increase) in the contribution of interfacial (shape) anisotropy. We then calculate the temperature dependence of Δ (curves in Fig. 2b) using modified Eq. (8) (see Methods for more details). At RT, the Δ of QUAD(5) is higher than that of DBL(15), but because DBL(15) has a smaller n, the Δ of DBL(15) is higher than that of QUAD(5) when T is above 150°C. While n of 2 is expected from the origin of shape anisotropy, n values related to interfacial anisotropy tend to be larger than three[55] due to device-fabrication-induced variation in magnetic properties at the vicinity of the device edge[56]. It is noteworthy that the impact of device fabrication is observed in the interfacial-anisotropy MTJs but not in the shape-anisotropy MTJ, suggesting that the bulk of a CoFeB layer has less impact on fabrication than a CoFeB/MgO interface[39,44]. The obtained results prove that tailoring MTJs to emphasize the shape anisotropy is effective for retention-critical applications.

Single-nanometer MTJs with high-speed capability

Next, we investigate STT switching with voltage pulse for various MTJ structures in the single-nanometer regime. Fig. 3a, b shows R as a function of pulsed voltage V for different pulse duration in representative MTJs with shape or interfacial anisotropies enhanced: SGL(15) with $D = 8.5$ nm and HEXA(2) with $D = 4.5$ nm, whose Δ are comparable (34 and 37, respectively). Switching is achieved at 1 µs and 100 ns in both structures. At shorter pulse duration, however, while HEXA(2) shows switching for both anti-parallel (AP) to parallel (P) states and vice versa at 10 ns, SGL (15) does not show switching from AP to P states. This can be explained by the increase in switching voltage in the precessional regime described earlier.

We then compare the trends of STT switching with respect to pulse duration between various structures. Fig. 3c shows V_C as a function of pulse duration for the MTJs presented in Fig. 3a, b (results for other MTJs are shown in Supplementary Information S3). Bidirectional switching with $\tau_p < 10$ ns is obtained for MTJs with $D < 5$ nm. To focus on the V_C increase at shorter pulse durations, V_C is normalized by the one at 1 µs for P to AP (AP to P) switching and plotted as a function of τ_p in Fig. 3d, e. While V_C does not change significantly in the range of 1 µs to 100 ns for both structures, the V_C increase at shorter pulse durations is more moderate in HEXA(2), where the interfacial anisotropy is dominant. We evaluate H_K^{eff} for studied structures from switching probability measurement under a magnetic field and summarize in Supplementary Information S4. We confirm that H_K^{eff} becomes larger by enhancing interfacial anisotropy as in HEXA(2) and OCTA(2). We then extract τ_D by fitting Eq. (3) to the experimental results in Fig. 3c, where Δ in Fig. 2a is used as a fixed parameter and τ_D is used as a fitting parameter. Note that the results obtained in our sample are well fitted by Eq. (3) with pulse durations up to 1 µs, even though Eq. (3) is valid in the precessional regime with a pulse

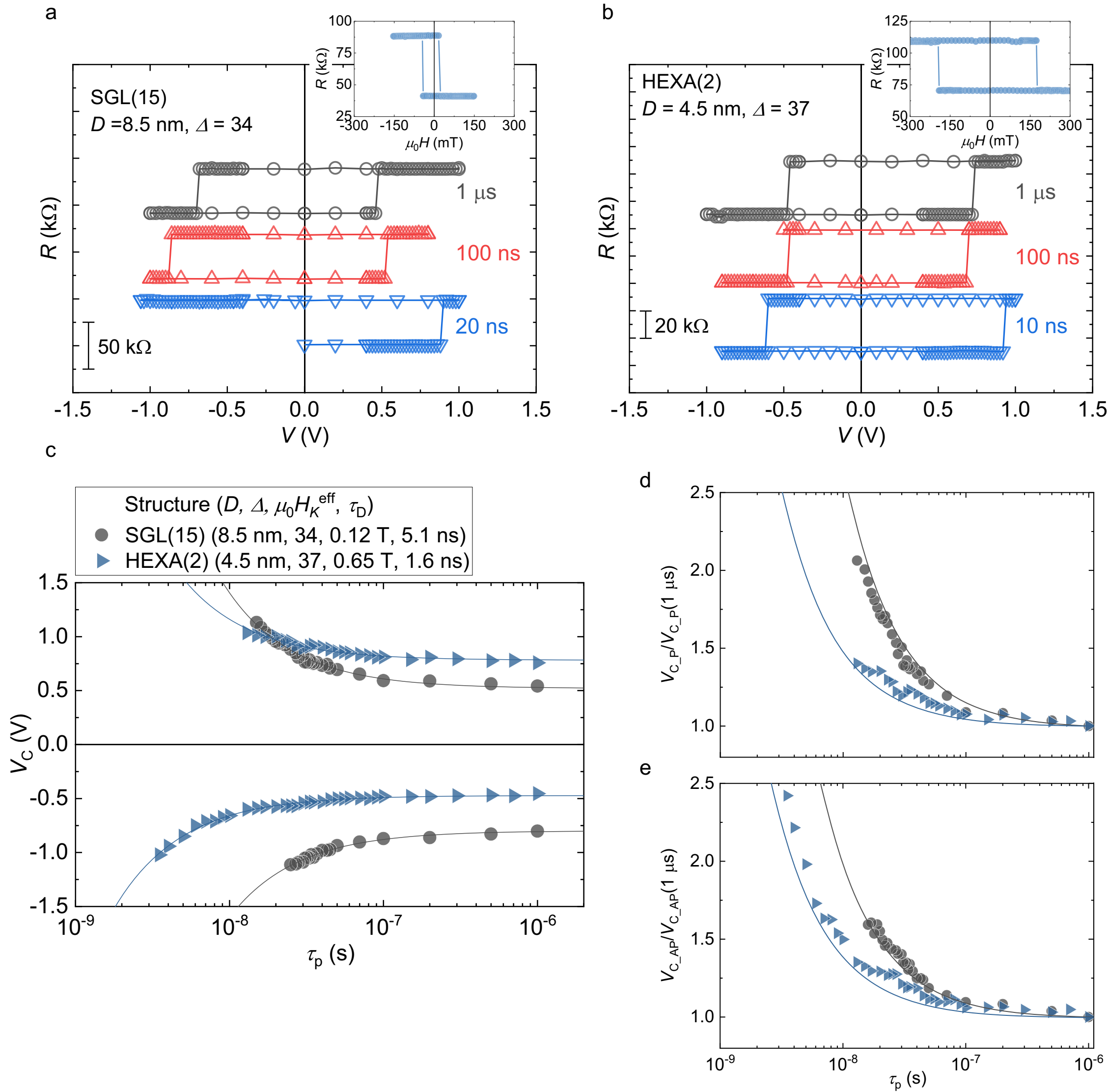

Fig. 3 STT switching measurement for SGL(15) with $D = 8.5$ nm and HEXA(2) with $D = 4.5$ nm. MTJ resistance R as a function of V: (**a**) for SGL(15) with $D = 8.5$ nm and (**b**) for HEXA(2) with $D = 4.5$ nm. Insets in (**a**) and (**b**) show R-H curves for the MTJ devices. **c** V_C with respect to pulse duration for different structures. Curves correspond to fitting curves using Eq. (3). **d**, **e** V_C for P to AP and AP to P switching (V_{C_P} and V_{C_AP}, respectively) normalized by that at 1 μs, respectively. Curves are normalized fitting curves obtained from (**c**). A part of data in (**c**), (**d**), and (**e**) is reproduced with permission from ref. [40]. Copyright 2021 IEEE.

duration up to about 10 ns according to previous studies[1,48,57]. The extracted τ_D is summarized with respect to $\mu_0 H_K^{eff}$ (from Fig. S4 in Supplementary Information S4) for various structures in Fig. 4. The τ_D decreases with increasing H_K^{eff} in consistent with Eq. (5), and fitting (Solid curve) yields $\alpha = 0.0139 \pm 0.0013$, which reasonably agrees with previous studies[25,58]. Note that the α value should be similar among studied structures. According to a previous study[58], α of the MgO/CoFeB/MgO system stays constant regardless of CoFeB thickness. We also evaluate N dependence of α using VNA-FMR in the multilayer and confirm that the increase in N does not affect α so much as well (see Supplementary Information S5). Most of the MTJs with shape anisotropy enhanced (red symbols) show larger τ_D and this fact explains the increase in V_C with decreasing τ_p below around 100 ns shown in Fig. 3c–e (see also Supplementary Information S3). On the other hand, short τ_D is obtained for those with interfacial anisotropy enhanced (blue symbols), explaining the high-speed switching shown in Fig. 3a–c (see also Supplementary Information S6). The obtained results prove that tailoring MTJs to emphasize the interfacial anisotropy is effective for fast STT switching.

DISCUSSION

This work uses a CoFeB/MgO material system with the multi-layered ferromagnetic structure to tailor device performance to applications requiring high data retention or high speed in a single-nanometer regime. Here we discuss how to improve device performance further in the proposed structures.

For Flash-like, or retention-critical, applications, one needs to maintain high retention property even at high temperatures. We demonstrate Δ over 70 at 150°C by enhancing shape anisotropy in multilayered ferromagnetic structure, which is enough for a single device. However, to satisfy the read error rate of 10^{-9} for 10^9-bit system[44], Δ needs to be over 80 at 85°C, 150°C, and 225°C for consumer, automobile, and solder-reflow process, respectively. Further increasing t_{CoFeB} and/or M_S by increasing Fe concentration in CoFeB layer[54] may achieve the required Δ.

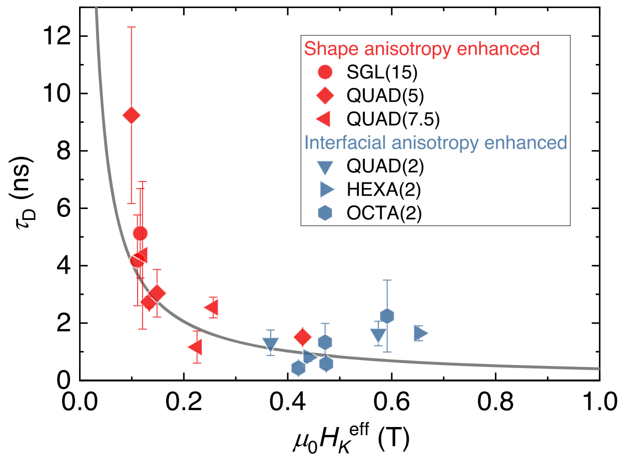

Fig. 4 Summarized τ_D as a function of $\mu_0 H_K^{eff}$ for each structure. Curve corresponds to Fitting using Eq. (5). The error bar shows the longest and shortest differences between both τ_D (for P to AP switching and AP-to-P switching), including standard errors, obtained by fitting using Eq. (3). Samples with shape (interfacial) anisotropy enhanced are indicated as red (blue) symbols.

For SRAM-like, or speed-critical, applications, one should suppress a rapid increase in write voltage at shorter τ_p for reliable high-speed switching. In our results, even though we achieve sub-ten-ns switching, we see a sizable increase in the switching voltage at the pulse duration shorter than 10 ns. Further V_C reduction in the precessional regime at the ultra-small scale can be expected by combining multilayered ferromagnetic structure and ultra-thin CoFeB layers[59,60]. Here we calculate STT switching voltage beyond 1 ns using Eqs. (3)–(5) considering a free layer of various materials/structures, shown in Fig. 5 (see Methods for the parameters used). For comparison, we also show calculated V_C for QUAD(2) and HEXA(2) (red curves). In all the free layers, we assume $D = 7.5$ nm and $\alpha = 0.005$. All the proposed free layers are expected to show smaller V_C than that of QUAD(2) and HEXA(2) owing to further enhancement of interfacial anisotropy. We especially reveal that the ultra-thin CoFeB layer, i.e., $[CoFeB(0.66)/MgO]_3$ (dashed blue curve) has the potential to achieve V_C of less than 1 V even at 1 ns. Another way for reliable high-speed switching is to introduce other materials with large K_b and low M_S such as $L1_0$-MnAl[61]. In our calculation, $L1_0$-MnAl (green curve) also has the potential to achieve V_C of less than 1 V even at 1 ns. Note that one needs to control α to avoid V_{C0} increase carefully. Apart from material/stack development of the free layer, introducing a double-spin MTJ structure[62,63] could also be another possibility to achieve reliable switching below 10 ns. Furthermore, this concept can be applied to devices operated with a spin-orbit torque (SOT)[64–66]. Since our approach is to increase the precessional frequency, the proposed stack could also be applied to three-terminal MTJs controlled by SOT[65,66] or a combination of STT and SOT[67–71].

In this study, we show CoFeB/MgO-based MTJ technology in the single-nanometer regime by introducing a multilayered ferromagnetic structure, which enables controlling interfacial and shape anisotropy independently at ultrafine scale. We show that emphasizing shape anisotropy allows sufficient thermal stability at high temperatures, whereas emphasizing interfacial anisotropy enables fast STT switching at 10 ns or below at ultrafine scale, which satisfies the requirement for Flash-like or SRAM-like applications. We also propose MTJ stacks that allow even faster switching with a lower voltage than studied MTJ stacks. This work provides design guideline to fabricate ultra-small MTJs used in a wide variety of applications.

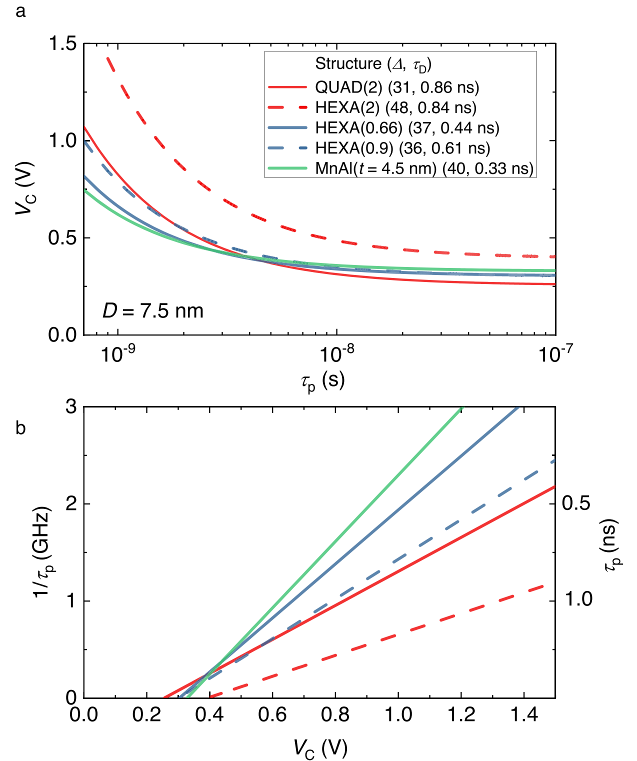

Fig. 5 Design of the free layer toward further high-speed operation. a Calculated V_C with respect to pulse duration for different structures using Eqs. (3) to (5). The parameters for HEXA(0.66), HEXA(0.9), and MnAl are based on the previous studies[58,60] (see Methods). **b** $1/\tau_p$ vs. V_C, replotted from (**a**) to see a difference in structures easily. The used parameters are shown in Methods.

METHODS

Sample preparation

The MTJ stacks were deposited on 3-inch thermally oxidized Si wafers by dc/rf magnetron sputtering system. The stacks are, from the substrate side, the followings: Ta(5)/Ru(10)/Ta(15)/Pt(5)/[Co(0.4)/Pt(0.4)]$_6$/Co(0.4)/Ru(0.4)/Co(0.4)/[Pt(0.4)/Co(0.4)]$_2$/Ta(0.2)/CoFeB(1)/MgO(1.0)/$(Co_{0.25}Fe_{0.75})_{75}B_{25}$(15.5)/Ta(5)/Ru(5) for SGL(15); Ta(5)/Ru(10)/Ta(t_{Ta})/Pt(5)/[Co(0.4)/Pt(0.4)]$_6$/Co(0.4)/Ru(0.4)/Co(0.4)/[Pt(0.4)/Co(0.4)]$_2$/Ta(0.2)/CoFeB(1)/MgO(t_{MgO})/[$(Co0._{25}Fe_{0.75})_{75}B_{25}$($t_{CoFeB}$)/MgO(0.93)]$_N$/Ru(5) with ($t_{Ta}$, t_{MgO}, t_{CoFeB}, N) = (15, 1.0 or 0.96, 15, 1), (15, 0.94, 5, 2), and (20, 0.94, 7.5, 2) for DBL(15), QUAD(5), and QUAD(7.5), respectively; and Ta(5)/Ru(10)/Ta(20)/Pt(5)/[Co(0.3)/Pt(0.4)]$_6$/Co(0.6)/Ru(0.4)/Co(0.6)/[Pt(0.4)/Co(0.3)]$_2$/W(0.2)/CoFeB(1)/MgO(t_{MgO})/[$(Co_{0.25}Fe_{0.75})_{75}B_{25}$(2)/MgO(0.93)]$_N$/Ru(5) with ($t_{MgO}$, N) = (0.98, 2), (0.94, 3), and (0.93, 4) for QUAD(2), HEXA(2), and OCTA(2), respectively. The numbers in the parentheses in the stacks are nominal thicknesses in nm. To suppress the increase in RA with increasing N and achieve as low RA as possible for STT switching, the MgO barrier thickness between the free and the reference layers was varied for each structure. Note that the impact of the increases in N on RA should be small; according to a previous study on DBL structure[72], the contribution of the top MgO layer to the total RA is less than 1 Ωμm^2. The stacks were processed into circular MTJs with various diameters by electron beam lithography, reactive ion etching, and multistep Ar ion milling[33]. After Ar ion milling, the MTJ was covered ex-situ with a SiN passivation layer using chemical vapor deposition. The processed wafers were post-annealed for 1 h (3 h) at 300°C for SGL(15), DBL(15), QUAD(5), and QUAD(7.5) (QUAD(2), HEXA(2), and OCTA(2)). MTJ diameters were electrically determined from the resistance (R)-area (A) product (RA) and the resistance of the parallel state of MTJs. RA of the studied MTJs is

summarized in Table 1. We used DBL(15) with $RA = 5.4$ (3.1) Ωμm^2 for the evaluation of Δ (STT switching). We used OCTA(2) with $RA = 1.1$ and 1.7 (1.0) Ωμm^2 for STT switching (TEM image shown in Fig. 1d and *R-H* curve shown in Fig. 1f).

Thermal stability measurement

We evaluated Δ and H_K^{eff} from switching probability measurement using a pulse magnetic field[51]. We applied the pulse magnetic field H_{pulse} 50 times. The measurements were carried out at temperatures from RT up to around 190°C[35,44]. We fitted the following equation to the experimental results with Δ, H_K^{eff}, and a shift field H_{shift} as fitting parameters,

$$P_{\mathrm{SW}}^{\mathrm{P(AP)}} = 1 - \exp\left\{-\frac{\tau_{\mathrm{pH}}}{\tau_0}\exp\left[-\Delta\left(1 \mp \frac{H_{\mathrm{pulse}} - H_{\mathrm{shift}}}{H_K^{\mathrm{eff}}}\right)^2\right]\right\} \quad (6)$$

where τ_{pH} is the pulse duration (= 1 s) of H_{pulse}, and τ_0 is the inverse of the attempt frequency (assumed to be 1 ns in this study).

Extraction of scaling exponent *n*

We extracted n in the same way as in ref. 44. From the temperature dependence of E ($\Delta k_B T$) and M_S, we obtained n as a slope of the following power law relationship:

$$\frac{E(T)}{E(T^*)} = \left\{\frac{M_S(T)}{M_S(T^*)}\right\}^n \quad (7)$$

where T^* is a normalizing temperature (RT in this study). We calculated the temperature dependence of M_S using Bloch law, $M_S(T) = M_{S0}(1 - aT^{3/2})$, where M_{S0} is M_S at 0 K and a is a material dependent parameter, providing M_{S0} of 1.59 T and a of 2.47×10^{-5} K$^{-3/2}$.

Calculation of *Δ* as a function of *T*

We calculated the temperature dependence of Δ (curves in Fig. 2c) using modified Eq. (7) as follows:

$$\Delta(T) = \Delta(T^*) \cdot \left(\frac{T^*}{T}\right) \cdot \left\{\frac{M_S(T)}{M_S(T^*)}\right\}^n \quad (8)$$

where $\Delta(T^*)$ is Δ at normalizing temperature (RT in this study). We took Δ from Fig. 2b into account Eq. (8). For the calculations, we used n values of 2.27, 3.44, and 2.58 for DBL(15), QUAD(5), and QUAD(7.5), respectively.

STT switching

We used a source meter to apply DC voltage and measure MTJ resistance for DC measurement. For high-speed measurement, we applied pulse voltage via rf port of bias-T and then measured MTJ resistance by source meter with reading voltage = 30 mV via dc port of bias-T. We measured switching probability with a pulse magnetic field.

The parameters used for the calculation of V_C

We calculated V_C shown in Fig. 5 under an assumption of either $[\mathrm{CoFeB/MgO}]_N$ multilayered ferromagnetic structure or $L1_0$-MnAl. The parameters used for calculation were as follows:

(1) $[\mathrm{CoFeB(2)/MgO}]_{2\ \mathrm{or}\ 3}$ (QUAD(2) or HEXA(2))
$M_S = 1.38$ T, $\alpha = 0.005$, $P = 0.4$, $K_b = 0$ J/m^3. $K_i = 3.48$ and 4.66 mJ/m^2 [40] for QUAD(2) and HEXA(2), respectively.

(2) $[\mathrm{CoFeB(0.66\ or\ 0.9)/MgO}]_3$ (HEXA(0.66) or HEXA(0.9))
$M_S = 1.70$ T, $\alpha = 0.005$, $P = 0.4$, $K_b = 0$ J/m^3, and $K_i = 4.44$ mJ/m^2 [59].

(3) $L1_0$-MnAl
$M_S = 0.60$ T, $\alpha = 0.005$, $P = 0.4$, $K_b = 8.5 \times 10^5$ J/m^3, and $K_i = 0$ mJ/m^2 [61].

DATA AVAILABILITY

The data that support the plots within this paper and other findings of this study are available from the corresponding author upon reasonable request.

Received: 2 August 2023; Accepted: 22 October 2023;
Published online: 04 January 2024

REFERENCES

1. Hosomi, M. et al. A novel nonvolatile memory with spin torque transfer magnetization switching: spin-ram. In *IEEE International Electron Devices Meeting, 2005. IEDM Technical Digest*. 459–462. https://doi.org/10.1109/IEDM.2005.1609379 (2005).
2. Kawahara, T., Ito, K., Takemura, R. & Ohno, H. Spin-transfer torque RAM technology: Review and prospect. *Microelectron. Rel.* **52**, 613–627 (2012).
3. Brataas, A., Kent, A. D. & Ohno, H. Current-induced torques in magnetic materials. *Nat. Mater.* **11**, 372–381 (2012).
4. Khvalkovskiy, A. V. et al. Basic principles of STT-MRAM cell operation in memory arrays. *J. Phys. D: Appl. Phys.* **46**, 074001 (2013).
5. Kent, A. D. A new spin on magnetic memories. *Nat. Nanotechnol.* **10**, 5 (2015).
6. Apalkov, D., Dieny, B. & Slaughter, J. M. Magnetoresistive random access memory. *Proc. IEEE* **104**, 1796–1830 (2016).
7. Oka, M. et al. 3D stacked CIS compatible 40 nm embedded STT-MRAM for buffer memory. In *2021 Symposium on VLSI Technology* 1–2 (2021).
8. Lee, K. et al. 28 nm CIS-compatible embedded STT-MRAM for frame buffer memory. In *2021 IEEE International Electron Devices Meeting (IEDM)* 2.1.1-2.1.4. https://doi.org/10.1109/IEDM19574.2021.9720537 (2021).
9. Natsui, M. et al. 12.1 An FPGA-Accelerated Fully Nonvolatile Microcontroller Unit for Sensor-Node Applications in 40 nm CMOS/MTJ-Hybrid Technology Achieving 47.14μW Operation at 200 MHz. In *Proc. 2019 IEEE International Solid- State Circuits Conference - (ISSCC)* 202–204. https://doi.org/10.1109/ISSCC.2019.8662431 (2019).
10. Naik, V. B. et al. Manufacturable 22 nm FD-SOI embedded MRAM technology for industrial-grade MCU and IOT applications. In *2019 IEEE International Electron Devices Meeting (IEDM)* 2.3.1-2.3.4. https://doi.org/10.1109/IEDM19573.2019.8993454 (2019).
11. Jung, S. et al. A crossbar array of magnetoresistive memory devices for in-memory computing. *Nature* **601**, 211–216 (2022).
12. Chiu, Y.-C. et al. A 22 nm 4 Mb STT-MRAM data-encrypted near-memory computation macro with a 192GB/s read-and-decryption bandwidth and 25.1-55.1TOPS/W 8b MAC for AI Operations. In *2022 IEEE International Solid- State Circuits Conference (ISSCC)* **65**, 178–180. https://doi.org/10.1109/ISSCC42614.2022.9731621 (2022).
13. Naik, V. B. et al. JEDEC-Qualified Highly Reliable 22 nm FD-SOI Embedded MRAM For Low-Power Industrial-Grade, and Extended Performance Towards Automotive-Grade-1 Applications. In *2020 IEEE International Electron Devices Meeting (IEDM)* 11.3.1-11.3.4. https://doi.org/10.1109/IEDM13553.2020.9371935 (2020).
14. Shih, Y.-C. et al. A Reflow-capable, Embedded 8 Mb STT-MRAM Macro with 9nS Read Access Time in 16 nm FinFET Logic CMOS Process. In *2020 IEEE International Electron Devices Meeting (IEDM)* 11.4.1-11.4.4. https://doi.org/10.1109/IEDM13553.2020.9372115 (2020).
15. Lee, P.-H. et al. 33.1 A 16 nm 32 Mb Embedded STT-MRAM with a 6 ns Read-Access Time, a 1M-Cycle Write Endurance, 20-Year Retention at 150°C and MTJ-OTP Solutions for Magnetic Immunity. In *2023 IEEE International Solid- State Circuits Conference (ISSCC)* 494–496. https://doi.org/10.1109/ISSCC42615.2023.10067837 (2023).
16. Alamdar, M. et al. Irradiation effects on perpendicular anisotropy spin orbit torque magnetic tunnel junctions. *IEEE Trans. Nucl. Sci.* **68**, 665 (2021).
17. Avalanche Technology. Avalanche Technology Announces Industry's First 1 Gb STT-MRAM For Aerospace Applications. https://www.avalanche-technology.com/avalanche-technology-announces-industrys-first-1gb-stt-mram-for-aerospace-applications/ (2021).
18. Ikegawa, S. et al. High-Speed (400MB/s) and Low-BER STT-MRAM Technology for Industrial Applications. In *2022 International Electron Devices Meeting (IEDM)* 10.4.1-10.4.4. https://doi.org/10.1109/IEDM45625.2022.10019513 (2022).
19. Seo, S. M. et al. First demonstration of full integration and characterization of 4F^2 1S1M cells with 45 nm of pitch and 20 nm of MTJ size. In *2022 IEEE International Electron Devices Meeting (IEDM)* 10.1.1-10.1.4. https://doi.org/10.1109/IEDM45625.2022.10019549 (2022).
20. Jinnai, B., Watanabe, K., Fukami, S. & Ohno, H. Scaling magnetic tunnel junction down to single-digit nanometers—Challenges and prospects. *Appl. Phys. Lett.* **116**, 160501 (2020).

21. Han, S. H. et al. 28-nm 0.08 mm2/Mb Embedded MRAM for Frame Buffer Memory. In *2020 IEEE International Electron Devices Meeting (IEDM)* 11.2.1-11.2.4. https://doi.org/10.1109/IEDM13553.2020.9372040 (2020).
22. Edwards, E. R. J. et al. Demonstration of narrow switching distributions in STTMRAM arrays for LLC applications at 1x nm node. In *2020 IEEE International Electron Devices Meeting (IEDM)* 24.4.1-24.4.4. https://doi.org/10.1109/IEDM13553.2020.9371985 (2020).
23. Lee, T. Y. et al. Advanced MTJ Stack Engineering of STT-MRAM to Realize High Speed Applications. In *2020 IEEE International Electron Devices Meeting* 11.6.1-11.6.4. https://doi.org/10.1109/IEDM13553.2020.9372015 (2020).
24. Mangin, S. et al. Current-induced magnetization reversal in nanopillars with perpendicular anisotropy. *Nat. Mater* **5**, 210–215 (2006).
25. Ikeda, S. et al. A perpendicular-anisotropy CoFeB–MgO magnetic tunnel junction. *Nat. Mater* **9**, 721–724 (2010).
26. Sato, H. et al. Perpendicular-anisotropy CoFeB-MgO magnetic tunnel junctions with a MgO/CoFeB/Ta/CoFeB/MgO recording structure. *Appl. Phys. Lett.* **101**, 022414 (2012).
27. Nishioka, K. et al. Novel Quad interface MTJ technology and its first demonstration with high thermal stability and switching efficiency for STT-MRAM beyond 2Xnm. In *2019 Symposium on VLSI Technology* T120–T121. https://doi.org/10.23919/VLSIT.2019.8776499 (2019).
28. Sato, H. et al. Properties of magnetic tunnel junctions with a MgO/CoFeB/Ta/CoFeB/MgO recording structure down to junction diameter of 11 nm. *Appl. Phys. Lett.* **105**, 062403 (2014).
29. Honjo, H. et al. 25 nm iPMA-type Hexa-MTJ with solder reflow capability and endurance > 10^7 for eFlash-type MRAM. In *2022 IEEE International Electron Devices Meeting (IEDM)* 10.3.1-10.3.4. https://doi.org/10.1109/IEDM45625.2022.10019412 (2022).
30. Lee, K. et al. 1Gbit High Density Embedded STT-MRAM in 28 nm FDSOI Technology. In *2019 IEEE International Electron Devices Meeting (IEDM)* 2.2.1-2.2.4. https://doi.org/10.1109/IEDM19573.2019.8993551 (2019).
31. Naik, V. B. et al. JEDEC-Qualified Highly Reliable 22 nm FD-SOI Embedded MRAM for low-power industrial-grade, and extended performance towards automotive-grade-1 applications. In *2020 IEEE International Electron Devices Meeting* 11.3.1-11.3.4. https://doi.org/10.1109/IEDM13553.2020.9371935 (2020).
32. Kim, D. S. et al. 28 nm CIS-Compatible Embedded STT-MRAM for Frame Buffer Memory. In *2021 IEEE International Electron Devices Meeting (IEDM)* 2.1.1-2.1.4. https://doi.org/10.1109/IEDM19574.2021.9720537 (2021).
33. Watanabe, K., Jinnai, B., Fukami, S., Sato, H. & Ohno, H. Shape anisotropy revisited in single-digit nanometer magnetic tunnel junctions. *Nat. Commun.* **9**, 663 (2018).
34. Perrissin, N. et al. A highly thermally stable sub-20 nm magnetic random-access memory based on perpendicular shape anisotropy. *Nanoscale* **10**, 12187–12195 (2018).
35. Jinnai, B. et al. High-Performance Shape-Anisotropy Magnetic Tunnel Junctions down to 2.3 nm. In *2020 IEEE International Electron Devices Meeting (IEDM)* 24.6.1-24.6.4. https://doi.org/10.1109/IEDM13553.2020.9371972 (2020).
36. Khanal, P. et al. Perpendicular magnetic tunnel junctions with multi-interface free layer. *Appl. Phys. Lett.* **119**, 242404 (2021).
37. Caçoilo, N. et al. Spin-torque-triggered magnetization reversal in magnetic tunnel junctions with perpendicular shape anisotropy. *Phys. Rev. Appl.* **16**, 024020 (2021).
38. Bendra, M. et al. Spin Transfer Torques in Ultra-Scaled MRAM Cells. in *2022 45th Jubilee International Convention on Information, Communication and Electronic Technology (MIPRO)* 129–132. https://doi.org/10.23919/MIPRO55190.2022.9803736 (2022).
39. Jinnai, B. et al. Coherent magnetization reversal of a cylindrical nanomagnet in shape-anisotropy magnetic tunnel junctions. *Appl. Phys. Lett.* **118**, 082404 (2021).
40. Jinnai, B. et al. Fast Switching Down to 3.5 ns in Sub-5-nm Magnetic Tunnel Junctions Achieved by Engineering Relaxation Time. In *2021 IEEE International Electron Devices Meeting (IEDM)* 2.6.1-2.6.4. https://doi.org/10.1109/IEDM19574.2021.9720509 (2021).
41. Automotive ElectronicsCouncil. AEC_Q100_Rev_H_Base_Document.pdf. *AEC-Q100-Rev-H.* http://www.aecouncil.com/Documents/AEC_Q100_Rev_H_Base_Document.pdf (2014).
42. Meng-Chun Shih et al. Reliability study of perpendicular STT-MRAM as emerging embedded memory qualified for reflow soldering at 260°C. In *2016 IEEE Symposium on VLSI Technology* 1–2. https://doi.org/10.1109/VLSIT.2016.7573411 (2016).
43. Gallagher, W. J. et al. 22 nm STT-MRAM for Reflow and Automotive Uses with High Yield, Reliability, and Magnetic Immunity and with Performance and Shielding Options. In *2019 IEEE International Electron Devices Meeting (IEDM)* 2.7.1-2.7.4. https://doi.org/10.1109/IEDM19573.2019.8993469 (2019).
44. Igarashi, J. et al. Temperature dependence of the energy barrier in X/1X nm shape-anisotropy magnetic tunnel junctions. *Appl. Phys. Lett.* **118**, 012409 (2021).
45. Perrissin, N. et al. Perpendicular shape anisotropy spin transfer torque magnetic random-access memory: Towards sub-10 nm devices. *J. Phys. D: Appl. Phys.* **52**, 234001 (2019).
46. Lequeux, S. et al. Thermal robustness of magnetic tunnel junctions with perpendicular shape anisotropy. *Nanoscale* **12**, 6378–6384 (2020).
47. Almeida, T. P. et al. Quantitative Visualization of Thermally Enhanced Perpendicular Shape Anisotropy STT-MRAM Nanopillars. *Nano Lett.* **22**(10), 4000–4005 (2022).
48. Bedau, D. et al. Spin-transfer pulse switching: From the dynamic to the thermally activated regime. *Appl. Phys. Lett.* **97**, 262502 (2010).
49. Liu, H. et al. Dynamics of spin torque switching in all-perpendicular spin valve nanopillars. *J. Magn. Magn. Mater.* **358–359**, 233–258 (2014).
50. Sun, J. Z. Spin-transfer torque switched magnetic tunnel junction for memory technologies. *J. Magn. Magn. Mater.* **559**, 169479 (2022).
51. Li, Z. & Zhang, S. Thermally assisted magnetization reversal in the presence of a spin-transfer torque. *Phys. Rev. B* **69**, 134416 (2004).
52. Sun, J. Z. Spin-current interaction with a monodomain magnetic body: A model study. *Phys. Rev. B* **62**, 570–578 (2000).
53. Wang, Z. et al. 22 nm Embedded STT-MRAM Macro with 10 ns Switching and >10^{14} Endurance for Last Level Cache Applications. in *2021 Symposium on VLSI Technology* 1–2 (2021).
54. Bersweiler, M., Sato, H. & Ohno, H. Magnetic and Free-Layer Properties of MgO/(Co)FeB/MgO Structures: Dependence on CoFeB Composition. *IEEE Magn. Lett.* **8**, 3109003 (2017).
55. Enobio, E. C. I., Bersweiler, M., Sato, H., Fukami, S. & Ohno, H. Evaluation of energy barrier of CoFeB/MgO magnetic tunnel junctions with perpendicular easy axis using retention time measurement. *Jpn. J. Appl. Phys.* **57**, 04FN08 (2018).
56. Naganuma, H., Sato, H., Ikeda, S. & Endoh, T. Micromagnetic simulation of the temperature dependence of the switching energy barrier using string method assuming sidewall damages in perpendicular magnetized magnetic tunnel junctions. *AIP Adv.* **10**, 075106 (2020).
57. Saino, T. et al. Write-error rate of nanoscale magnetic tunnel junctions in the precessional regime. *Appl. Phys. Lett.* **115**, 142406 (2019).
58. Okada, A. et al. Magnetization dynamics and its scattering mechanism in thin CoFeB films with interfacial anisotropy. *Proc. Natl. Acad. Sci. USA* **114**, 3815–3820 (2017).
59. Iwata-Harms, J. M. et al. Ultrathin perpendicular magnetic anisotropy CoFeB free layers for highly efficient, high speed writing in spin-transfer-torque magnetic random access memory. *Sci. Rep.* **9**, 19407 (2019).
60. Santos, T. S. et al. Ultrathin perpendicular free layers for lowering the switching current in STT-MRAM. *J. Appl. Phys.* **128**, 113904 (2020).
61. Takeuchi, Y. et al. Nanometer-thin $L1_0$-MnAl film with *B*2-CoAl underlayer for high-speed and high-density STT-MRAM: Structure and magnetic properties. *Appl. Phys. Lett.* **120**, 052404 (2022).
62. Hu, G. et al. STT-MRAM with double magnetic tunnel junctions. In *2015 IEEE International Electron Devices Meeting (IEDM)* 26.3.1-26.3.4. https://doi.org/10.1109/IEDM.2015.7409772 (2015).
63. Hu, G. et al. 2X reduction of STT-MRAM switching current using double spin-torque magnetic tunnel junction. In *2021 IEEE International Electron Devices Meeting (IEDM)* 2.5.1-2.5.4. https://doi.org/10.1109/IEDM19574.2021.9720691 (2021).
64. Miron, I. M. et al. Perpendicular switching of a single ferromagnetic layer induced by in-plane current injection. *Nature* **476**, 189–193 (2011).
65. Liu, L. et al. Spin-torque switching with the giant spin hall effect of tantalum. *Science* **336**, 555–558 (2012).
66. Fukami, S., Anekawa, T., Zhang, C. & Ohno, H. A spin–orbit torque switching scheme with collinear magnetic easy axis and current configuration. *Nat. Nanotech.* **11**, 621–625 (2016).
67. Wang, M. et al. Current-induced magnetization switching in atom-thick tungsten engineered perpendicular magnetic tunnel junctions with large tunnel magnetoresistance. *Nat. Commun.* **9**, 671 (2018).
68. Sato, N., Xue, F., White, R. M., Bi, C. & Wang, S. X. Two-terminal spin–orbit torque magnetoresistive random access memory. *Nat Electron* **1**, 508–511 (2018).
69. Grimaldi, E. et al. Single-shot dynamics of spin–orbit torque and spin transfer torque switching in three-terminal magnetic tunnel junctions. *Nat. Nanotechnol.* **15**, 111–117 (2020).
70. Krizakova, V., Garello, K., Grimaldi, E., Kar, G. S. & Gambardella, P. Field-free switching of magnetic tunnel junctions driven by spin–orbit torques at sub-ns timescales. *Appl. Phys. Lett.* **116**, 232406 (2020).
71. Zhang, C., Takeuchi, Y., Fukami, S. & Ohno, H. Field-free and sub-ns magnetization switching of magnetic tunnel junctions by combining spin-transfer torque and spin–orbit torque. *Appl. Phys. Lett.* **118**, 092406 (2021).
72. Mihajlović, G. et al. Origin of the resistance-area-product dependence of spin-transfer-torque switching in perpendicular magnetic random-access memory cells. *Phys. Rev. Appl.* **13**, 024004 (2020).

ACKNOWLEDGEMENTS
The authors would like to thank Y. Takeuchi, V. Desbuis, I. Morita, R. Ono, and M. Musya for fruitful discussion and technical support. This work was partly supported by JST-OPERA JPMJOP1611; JSPS KAKENHI JP19K04486 and JP19J12926; Cooperative Research Projects of RIEC, Tohoku University; and DIARE of Tohoku University. J.I. acknowledges financial support from GP-Spin of Tohoku University and JST-OPERA.

AUTHOR CONTRIBUTIONS
J.I., B.J., S.F., and H.O. planned study. J.I. and B.J. fabricated MTJs. J.I., B.J., and T.S. performed measurements. J.I. performed calculation. K.W., T.F., and H.S. characterized the coupling in multilayered ferromagnetic structures. K.W. evaluated the damping constant. J.I., B.J., and S.F. wrote manuscript with input from H.S. and H.O. All authors discussed the results.

COMPETING INTERESTS
The authors declare no competing interests.

ADDITIONAL INFORMATION
Supplementary information The online version contains supplementary material available at https://doi.org/10.1038/s44306-023-00003-2.

Correspondence and requests for materials should be addressed to Butsurin Jinnai or Shunsuke Fukami.

Reprints and permission information is available at http://www.nature.com/reprints

Publisher's note Springer Nature remains neutral with regard to jurisdictional claims in published maps and institutional affiliations.

Open Access This article is licensed under a Creative Commons Attribution 4.0 International License, which permits use, sharing, adaptation, distribution and reproduction in any medium or format, as long as you give appropriate credit to the original author(s) and the source, provide a link to the Creative Commons license, and indicate if changes were made. The images or other third party material in this article are included in the article's Creative Commons license, unless indicated otherwise in a credit line to the material. If material is not included in the article's Creative Commons license and your intended use is not permitted by statutory regulation or exceeds the permitted use, you will need to obtain permission directly from the copyright holder. To view a copy of this license, visit http://creativecommons.org/licenses/by/4.0/.

© The Author(s) 2024